Biomaterials Science

ROYAL SOCIETY OF CHEMISTRY

PAPER

View Article Online
View Journal | View Issue

Cite this: *Biomater. Sci.*, 2022, **10**, 1209

A theranostic microneedle array patch for integrated glycemia sensing and self-regulated release of insulin†

Xuetong Sun,[a] Wenwen Ji,[a] Bei Zhang,[a] Lijuan Ma,[a] Wenjuan Fu,[a] Wenhui Qian,[a] Xiangying Zhang,[a] Jianting Li,[a] Enze Sheng, *[a] Yi Tao*[b] and Dong Zhu *[a]

Received 30th November 2021,
Accepted 16th January 2022

DOI: 10.1039/d1bm01834e

rsc.li/biomaterials-science

Diabetes can cause various complications and affect the normal functioning of the human body. A theranostic and diagnostic platform for real-time glycemia sensing and simultaneous self-regulated release of insulin is desired to improve diabetic patients' life quality. Here, we describe a theranostic microneedle array patch, which enables the achievement of visualization quantification of glycemia and simultaneously self-regulated release of insulin. The microneedle patch (MNDF) was fabricated by crosslinking of 3-aminophenylboronic acid (ABA)-modified sodium alginate and chondroitin sulfate. The hierarchical structure consisted of a tip part containing mineralized insulin particles and glucose oxidase (GOD) for insulin release, and a base surface embodying 3,3′,5,5′-tetramethylbenzidine (TMB) and (horseradish peroxidase) HRP for real-time glycemia sensing. In the presence of glucose, GOD converts glucose into H^+ and H_2O_2, driving gradual dissolution of the calcium layer of insulin particles, resulting in long-acting release of insulin. By the bio-catalytic action of HRP, the generated H_2O_2 brings about a visible color change allowing the glucose level at the base surface to be read out. We believe that the theranostic microneedle array patch can act as a promising alternative for future clinical applications.

Introduction

Diabetes mellitus, as a widespread chronic metabolic disease,[1,2] can lead to a series of complications such as blindness, renal failure, circulatory problems and stroke.[3,4] It is also one of the top ten causes of adult death.[5] Such patients with type 1 and type 2 diabetes can achieve normal blood glucose by injection or infusion of insulin to prevent some complications of diabetes.

In recent years, plenty of studies have been conducted to develop a microneedle insulin delivery system.[6] The use of a microneedle, as a kind of convenient drug delivery device, penetrating the corneous layer for drug delivery is a painless and minimally invasive approach that will not harm the subcutaneous tissue. To date, solid microneedles,[7] hydrogel microneedles,[8] coated microneedles,[9] and hollow microneedles[10] have been developed for transdermal drug treatment. Compared with other microneedles, hydrogel microneedles have attracted much attention because of their excellent biosafety and drug release ability.

Common hydrogel microneedles are mainly composed of soluble or biodegradable and water-swellable polymers,[11–14] including gelatin, hyaluronate and polyvinyl alcohol. These microneedles generally utilize one of the various mechanisms of biochemical reactions, based on glucose binding proteins (GBP),[15] glucose response copolymer phenylboronic acid (PBA),[8,16–19] glucose oxidase (GOD),[20–23] and hypoxia triggers,[24] respectively.[25] Generally, hydrogel microneedles do not produce sharp medical waste, and their disposable characteristics enable reducing the possible spread of infection. However, pure hydrogel microneedles still face great challenges in long-term control of blood glycemia levels. The non-self-regulated release of insulin and the complex manufacturing process also limited their further applications.[26] More importantly, the therapeutic effect after microneedle administration cannot be evaluated simultaneously, in which, the blood glycemia level is usually tested with only special equipment or in hospitals after needle sampling. This increases the complexity of the user's operation and the risk of infection.

Here, we designed a hierarchically structured microneedle patch (MNDF) by cross-linking of ABA-modified sodium alginate and chondroitin sulfate, which has enough mechanical strength to penetrate the skin. The MNDF enables providing

[a]*School of Pharmacy, Nanjing University of Chinese Medicine, Nanjing, Jiangsu 210023, P. R. China. E-mail: 300563@njucm.edu.cn, dongzhu@njucm.edu.cn*
[b]*College of Pharmaceutical Science, Zhejiang University of Technology, Hangzhou, 6310014, China. E-mail: taoyi1985@zjut.edu.cn*

†Electronic supplementary information (ESI) available. See DOI: 10.1039/d1bm01834e

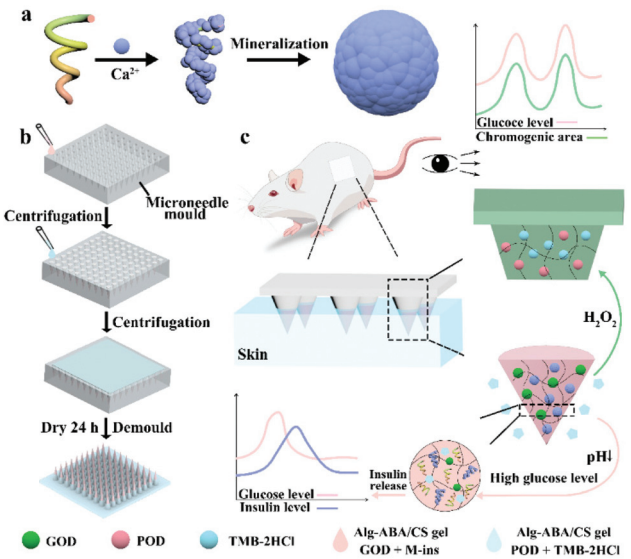

Scheme 1 Schematic of glucose responsiveness for triggering self-regulated release of insulin and real-time glycemia sensing with the naked eye. (a) Mineralization of insulin by Ca^{2+}. (b) Bi-functional microneedle array patch prepared by crosslinking and micro-molding. (c) Triggering self-regulated release of insulin and real-time glycemia sensing by glucose responsiveness.

dual-function for self-regulated insulin delivery and simultaneous glycemia sensing. As shown in Scheme 1, the tip component of this microneedle contains mineralized insulin particles and GOD that converts glucose into H^+ and H_2O_2. The calcium layer of insulin particles gradually dissolves under the acidic pH generated, so that the insulin enables effective long-acting release. On the other hand, the base surface of this microneedle embodies 3,3′,5,5′-tetramethylbenzidine (TMB) and (horseradish peroxidase) HRP, brings about a visible color change allowing the glucose level in the presence of H_2O_2 produced by the reaction at the needle tip to be read out. What's more, excessive H_2O_2 produced in the first reaction can be scavenged through this design – similar to an effective strainer – avoiding possible damage to normal tissues caused by oxidative stress. The MNDF has good glucose responsiveness for triggering self-regulated release of insulin and real-time glycemia sensing with the naked eye. As a portable diagnosis and treatment device, the MNDF has high biocompatibility and a simple manufacturing process, showing tremendous potential for further clinical application.

Results and discussion

Construction and characterization of MNDF

The MNDF is fabricated through a crosslinking by 3-aminophenylboronic acid (ABA)-modified alginate (Alg-ABA) and chondroitin sulfate (CS), in which the modification of ABA to alginate is designed to provide a phenylboronic acid to form a bond with the hydroxy functional group in CS, resulting in successful crosslinking. As shown in Fig. S1A and S1B,† the signal of phenyl groups (7.0–8.0 ppm) could be observed in the ^1H NMR spectrum of Alg-ABA, indicating that 3-aminophenylboronic acid was successfully grafted onto alginate. The crosslinking could provide sufficient mechanical strength for penetrating the skin, and also extend the release period of encapsulated insulins to disperse into skin tissue. As shown in Fig. 1A and B, each needle had a pyramidal shape, with a bottom width of about 400 μm and a height of about 600 μm, and the tip diameter was approximately 35 μm. The mechanical strength of this MNDF was tested by recording the pressure displacement curve by pressing the needle on the stress gauge through a stainless steel plate. Fig. 1C shows the stress–strain curves of MNDF. The stress of MNDF reaches 0.49 N per needle, five times the force for successfully inserting into the skin barrier (0.098 N per needle),[27] indicating that the MNDF

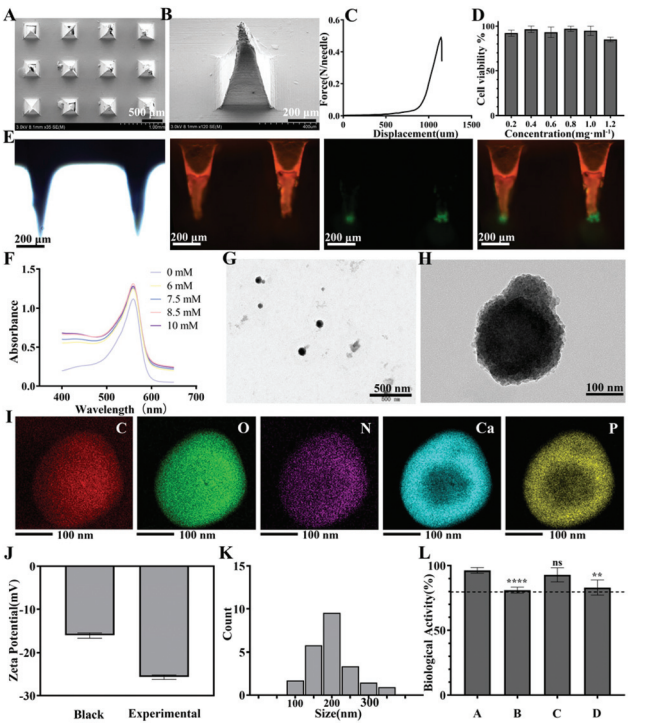

Fig. 1 Characterization and images of the MNDF. (A) SEM image of the top view of a microneedle. (B) SEM image of the side view of the microneedle. Scale bar: 500 μm in (A) and 200 μm in (B). (C) The stress–strain curve of the MNDF. (D) The cytotoxicity study of the MNDF. Mean ± SD (n = 3). (E) Fluorescence microscopy images of the needles containing Rho B-POD and FITC-insulin. Scale bar: 200 μm. (F) UV absorption spectrograms of the M-insulin during the bio-mineralization in different concentrations of calcium and insulin of 1.67 mg mL^{-1}. (G) and (H) TEM images of M-insulin nanoparticles. Scale bar: 500 nm in (G) and 100 nm in (H). (I) The elemental mapping of the M-insulin. Scale bar: 100 nm. (J) Zeta potential characterization of insulin and M-insulin. Mean ± SD (n = 3). (K) Size distribution of M-insulin by Nanoparticle Tracking Analysis (NTA). (L) Bioactivity of M-insulin (after 12 h of storage at 37 °C, A: M-insulin, B: M-insulin mixed with the Alg-ABA/CS complex, C: M-insulin embodied in the MNDF, and D: after 24 h of storage at 37 °C, M-insulin embodied in the MNDF). Mean ± SD (n = 4). The symbols above the bars represent the differences in the bioactivity of M-insulin in groups B, C, D and A (**P < 0.01, ****P < 0.0001).

has enough mechanical strength to penetrate the skin. The cytotoxicity of MNDF was accessed by performing CCK-8 viability assay. As shown in Fig. 1D, the cell viability was maintained above 92% in the MNDF range of 0.2–1.0 mg mL^{-1}, and 85% at 1.2 mg mL^{-1}; these results indicated that the prepared MNDF had excellent biological compatibility.

To validate the feasibility of the hierarchical structure on MNDF, rhodamine-labeled peroxidase (Rho-POD) and fluorescein isothiocyanate-labeled insulin (FITC-insulin) had been introduced into the MNDF in the preparation process, to distinguish the two layers (one is the layer for insulin release and the other is the layer for real-time glycemia sensing). Obviously, both the red layer (representing the sensing unit) and green layer (representing the insulin releasing unit) were observed in every needle; moreover, the green and red signals scarcely overlapped (Fig. 1E), verifying the separate integration. These results demonstrated the feasibility of preparing dual-functional MNDF arrays, with a needle tip layer for self-regulated release of insulin and a bottom layer for real-time glycemia sensing.

Fabrication and characterization of biomineralized insulin

The mineralization of insulin was conducted in the presence of calcium, and the corresponding insulin nanoparticles (M-insulin) were fabricated in CO_2 medium. According to the ultraviolet-visible (UV-vis) absorption spectra (Fig. 1F), when the Ca concentration was increased to 8.5 mM, the maximum absorbance without an absorption peak shift was observed, indicating that there was hardly any derangement for solution equilibrium. The morphology of M-insulin was ultimately 200 nm nanoparticles as determined by transmission electron microscopy (TEM) as shown in Fig. 1G and H. Energy dispersive spectroscopy (EDS) was used for elemental analysis of the complex to further confirm its composition. C, O and N were uniformly distributed throughout the nanoparticles, whereas Ca and P were mainly distributed on the periphery of the nanoparticles, and they were the main elements that constituted the particles, suggesting calcium–insulin complex formation, Fig. 1I. According to the zeta potential results, the values decreased from −16.0 ± 0.5 mV to −25.6 ± 0.4 mV (Fig. 1J). The carbon dioxide in the reaction system sustained the reaction and led to the production of M-insulin particles with relatively more negative charge.[28] In addition, Fourier transform infrared (FTIR) spectroscopy demonstrated that Ca ions and insulin were successfully complexed. In the composite M-insulin, the C═O stretching vibration of the amide of insulin at 1516 cm^{-1} and 1656 cm^{-1} moved to 1537 cm^{-1} and 1650 cm^{-1}, and a new absorption peak appeared at 1036 cm^{-1} owing to inorganic phosphate peaks (stretching vibration of P–O). These vibration peaks confirmed the synthesis of M-insulin (Fig. S2†). No obvious difference in their biological activity was found between the M-insulin and M-insulin loaded in MNDF (Fig. 1L). After 12 h of storage at 37 °C, the bioactivity of M-insulin was only reduced by 4%, while the bioactivity of the M-insulin mixed with the Alg-ABA/CS complex under the same conditions was 81%, and the corresponding bioactivity of M-insulin embodied in the MNDF was 93%. Moreover, the bioactivity of the released insulin from the M-insulin embodied in the MNDF after storage at 37 °C for 24 h, was still above 80%. For M-insulin, encapsulation into MNDF had no obvious adverse effect on bioactivity.

Evaluation of the *in vitro* effects of MNDF

As shown in Fig. 2A, the skin was successfully punctured through histological observations displaying a lacerated stratum corneum. The depositing of green dye at the MNDF puncture site indicated an effective local release of FITC-insulin from the implanted MNDF, and the maximum releasing depth of FITC-insulin was nearly 1 mm. After penetrating the MNDF into an agarose gel containing different glucose concentrations, a remarkable color difference was observed (Fig. 2B). Fig. 2C shows that the chromaticity coordinates of MNDF were mostly distributed in the green area. An analysis of the RGB histogram by using ImageJ could provide the corresponding quantification information. With the increase of glucose concentrations, the color of MNDF turned deeper, and the RGB value also showed varying degrees of drop with a shifting rate of red (from 213 to 84) > green (from 201 to 82) > blue (from 175 to 64), resulting in the appearance of a greener color to the naked eye, which can be used to judge the glucose levels as shown in Fig. 2D.

To check the feasibility of the glucose-triggering characteristic, GOD was added to different concentrations of glucose solutions which included a control group (0 mg dL^{-1}), a normglycemic group (100 mg dL^{-1}) and a hyper-glycemic group (400 mg dL^{-1}). Evidently, glucose oxidation catalysis reaction in the presence of GOD was modulated with concentration-dependent properties. Within 40 min, a high glucose level (400 mg dL^{-1}) generated a larger pH decrease (pH 7.1 to 4.6), while the control (0 mg dL^{-1}) or normal glucose concentration (100 mg dL^{-1}) induced a slight pH change (Fig. 2E). Moreover, M-insulin particles dissociate quickly when the pH is significantly below 6,[28] which was confirmed by NTA measurements (Fig. 2F). When the solution pH is 7.4, the average particle diameter is about 180 nm. When the pH is decreased to 6.2 and 4.0, the average particle diameter is also changed to 120 nm and 80 nm, respectively. Next, the release rate of insulin from M-insulin was tested at three different glucose concentrations. Under 100 mg dL^{-1} glucose, the amount of insulin released within 60 min was 111 μg mL^{-1}, while with 400 mg dL^{-1} glucose, the insulin release was promoted rapidly to 263 μg mL^{-1} as shown in Fig. 2G.

Evaluation of the ability of MNDF to detect hyperglycemia in rats

As shown in Fig. 3A and B, the skin damage caused by MNDF was negligible and could be self-recovered within 50 min. We evaluated the *in vivo* theranostic capability of the MNDF in an insulin-deficient streptozotocin (STZ) induced diabetic rat. The microneedle was penetrated into the rat's skin, and the initial colorless microneedle began to generate a green color on the

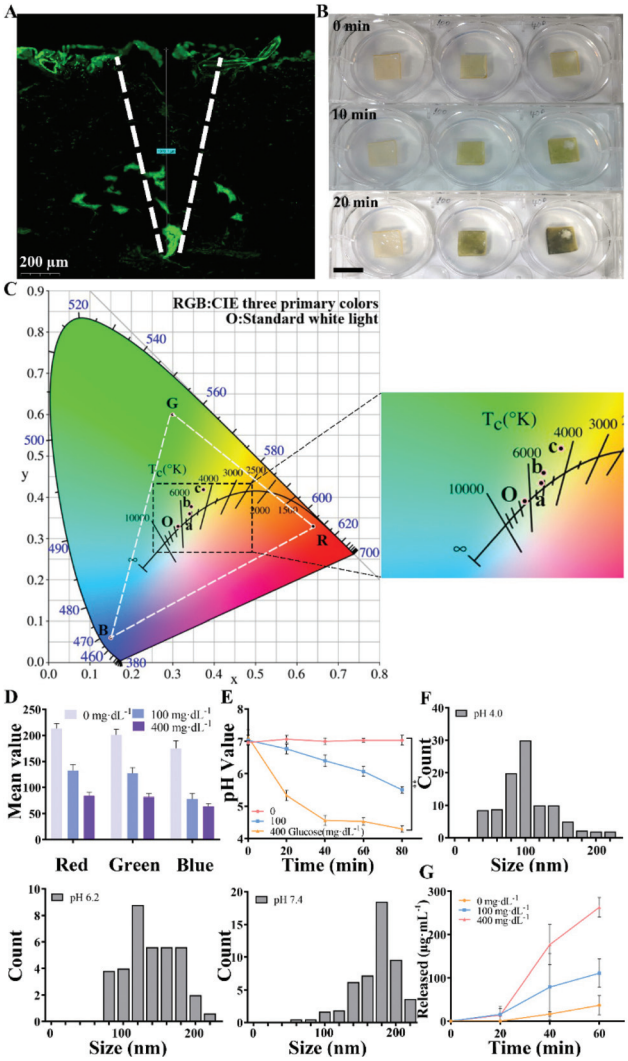

Fig. 2 *In vitro* glucose real-time responsive color change and mineralized particle release analysis from MNDF. (A) Histological sections of porcine skin after application of MNDF containing FITC-insulin. Scale bar: 200 μm. (B) Image of the MNDF color change in 2 wt% agarose hydrogel that simulates interstitial fluid extraction containing various glucose concentration solutions (from left to right, the glucose concentration was 0, 100, and 400 mg dL^{-1}, respectively). Scale bar: 1 cm. (C) The color of MNDF in International Commission on illumination 1931 (CIE 1931) chromaticity spaces (a, b, and c correspond to the color of MNDF under different glucose environments (0 mg dL^{-1}, 100 mg dL^{-1}, and 400 mg dL^{-1}) at 20 min, respectively). (D) The mean RGB value of images in (B) 20 min. Mean ± SD (n = 3). (E) The pH decreases in several glucose solutions containing the GOD (0.2 mg mL^{-1}). Mean ± SD (n = 3). (F) The particle size of M-insulin at different pH values. (G) At 37 °C, the concentration-dependent *in vitro* cumulative insulin release of MNDF at different glucose concentrations. Mean ± SD (n = 3) (**P < 0.01).

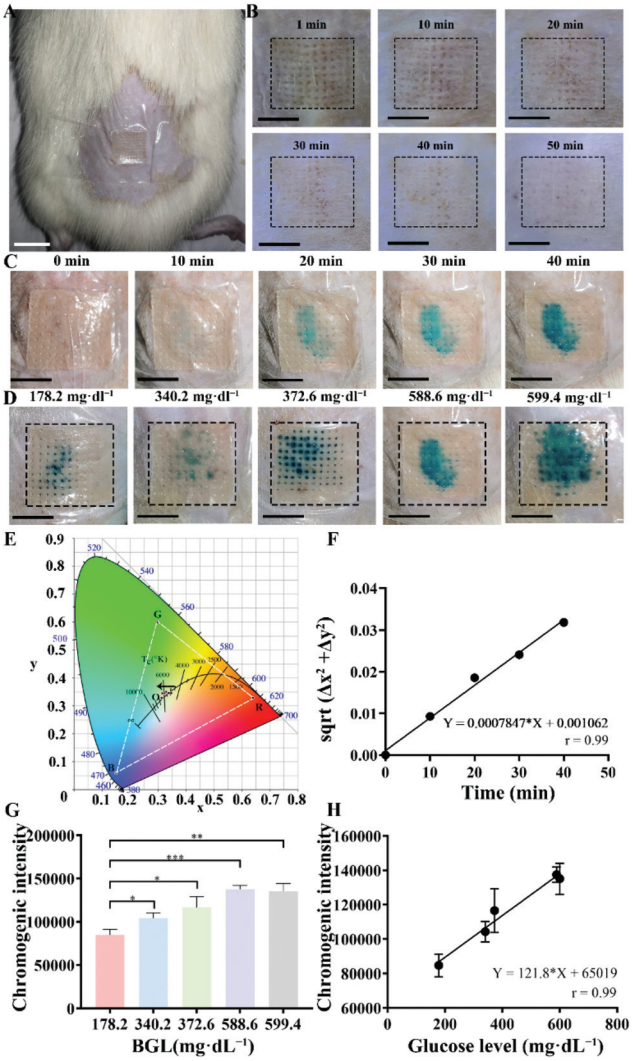

Fig. 3 The animal experiments by using the MNDF in living SD rats. (A) The MNDF was pressed into the skin of the rat and then fixed with a tegaderm film (3 M). Scale bar: 1 cm. (B) The skin recovery after the penetration: the hole marks caused by MNDF gradually became invisible within 50 min. Scale bar was 5 mm. (C) Images of the MNDF color changing at different points in time of diabetic rats. Scale bar was 5 mm. (D) Images of the MNDF color change at different BGLs of diabetic rats. Scale bar was 5 mm. (E) The CIE 1931 chromaticity diagram shows that the MNDF color in (C) shifts over time. (F) Linear relationship between the MNDF color shift distance and time. (G) Chromogenic intensity of the MNDF in (D) analyzed with ImageJ software. Mean ± SD (n = 3). (H) The linear fitting equation between the blood glucose level and MNDF chromogenic intensity. The error bars represent the standard deviation of three independent measurements (*P < 0.05, **P < 0.01, ***P < 0.001).

diabetic rat in 10 min, and the color no longer changed after 40 min, indicating the reaction balance (Fig. 3C).

Notably, as the blood glucose levels (BGLs) of diabetic rats were different, the chromogenic status of the MNDF was BGL-dependent. A high blood glucose level (such as 599.4 mg dL^{-1}) induced a deeper chromogenic area of the microneedles, while a normal blood glucose level (such as 178.2 mg dL^{-1}) only resulted in slight color changes (Fig. 3D). As shown in Fig. 3E and F, the chromaticity coordinates of MNDF gradually move to the green area with the increase of time, and an excellent linear relationship was achieved between the time and color shift distance. The regression equation was $Y = 0.0007847 \times X + 0.001062$, $r = 0.99$. The blood glucose level of the rats was

tested using a blood glucose meter at the same time, and the correlation analysis was carried out with the chromogenic intensity of the MNDF (calculated with ImageJ software, Fig. 3G). A linear fitting equation with the correlation coefficient r = 0.99 was obtained (Fig. 3H), and the detection limit was 160.3 mg dL^{-1}. Compared with the lowest hyperglycemia level (200 mg dL^{-1}), the detection limit of MNDF was lower than the threshold of hyperglycemia, which was sufficient for the discrimination of hyperglycemia.

Evaluation of the ability of MNDF to treat hyperglycemia in rats

To validate the *in vivo* therapy effect of the MNDF, the animals were randomly assigned to six groups: diabetic SD rats through an intraperitoneal injection (5 U), diabetic SD rats through MNDF compresses (5, 10 and 20 U), the control diabetic SD rat group through blank MNDF compresses and the healthy group (SD rats without diabetes). A stable diabetic model was successfully established through pathological examinations of the pancreas and kidneys of rats and high BGLs (Fig. S3†).

The BGL of each group was tested over time. Clearly, in the untreated control group, minimal fluctuations of the BGL (~346.2 ± 16.2 to 400.8 ± 25.6 mg dL^{-1}) were observed (Fig. 4A). As expected, all of the BGLs in rats treated with free insulin and MNDF decreased to below 200 mg dL^{-1} (Fig. 4A). The BGLs of diabetic rats decreased by 61.2% (from approximately 399 to 155.4 mg dL^{-1}) within 1 h when free insulin was administered; however, this norm-glycemic state was not maintained over 2.8 h, instead, due to the fast clearance of the drug, the BGL returned to a hyperglycemic state after 3.8 h. In contrast, the therapy with the MNDF containing mineralized particles (MN/M-insulin) exhibited promising BGL control, and the MNDF enabled regulation of the BGL within the aimed range (<200 mg dL^{-1}) for more than 4 h. Enzyme-linked immunosorbent assay (ELISA) revealed a continuous replenishment of plasma insulin under MNDF treatment (Fig. 4B). Different from direct injection of insulin, the MNDF (10 U, 20 U) still releases insulin continuously after 1 h, and reaches the maximum release at 4 h. This result can be clearly confirmed by the area under the curve (AUC) shown in Fig. 4C. Comparing the acting time of different hydrogel microneedles, MNDF shows better glycemia control ability (Table S1†).

Moreover, in contrast to intraperitoneal injection, even if the MNDF was administered in a normoglycemic rat, the corresponding BGL was maintained at 105 mg dL^{-1}, while the blood glucose of rats directly injected with insulin decreased to 42 mg dL^{-1} (Fig. 4D). Through the analysis of the hypoglycemia index (denoted as the decline value from the initial blood glucose to the minimum blood glucose divided by the time to reach the drop) (Fig. 4E),[27] insulin injection alone will cause a large drop in blood glucose, while MNDF administration greatly reduces the risk of hypoglycemia and ensures the safety of MNDF treatment.

Table 1 displays the pharmacokinetic parameters of the plasma insulin levels. The relative bioavailability (RBA) of the MNDF was evaluated to be 97.96% ± 5.52% compared with that in the case of intraperitoneal injection of insulin. These results proved the validity of the MNDF and that insulin can show a smooth self-regulated release from MNDF without any loss of activity.

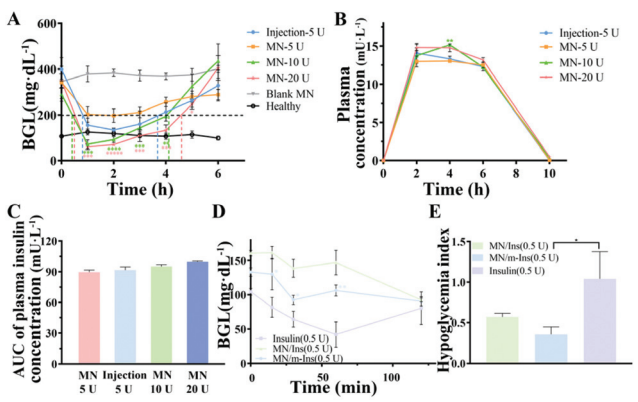

Fig. 4 (A) BGL monitoring in diabetic rats under different treatments. (B) Curves of plasma insulin concentration with time for different treatments. (C) Area under the curve (AUC) of plasma insulin concentration. (D) Blood sugar changes of healthy rats treated with insulin, MNDF/m-insulin, and MNDF/insulin. (E) Quantification of the hypoglycemia index in (D). Mean ± SD (n = 3). (*P < 0.05, **P < 0.01, ***P < 0.001, ****P < 0.0001, and *****P < 0.00001).

Experimental

Synthesis of Alg-ABA

The synthesis of Alg-ABA was performed as in a previous report.[29] Sodium alginate (1 g), NHS (0.46 g) and 3-aminophenylboronic acid (0.39 g) were added to deionized water (100 mL) and activated for 4 h. Then EDC·HCl was added (0.96 g) and stirred at room temperature for 12 h, dialyzed with a 3500 Da dialysis bag to remove excess EDC and NHS, and the water was changed every 6 hours. Finally, the product was lyophilized to a constant weight, and the prepared Alg-ABA solid was stored at 4 °C for later use. The composition of Alg-ABA was characterized by ^{1}H-NMR (Fig. S1†).

Fabrication of sodium alginate-3-aminobenzeneboronic acid/chondroitin sulfate (Alg-ABA/CS) dual-function MNDF

The MNDF was fabricated using a polydimethylsiloxane (PDMS) mold (Microneedle Technologies Pte Ltd, Singapore).

Table 1 Pharmacokinetic parameters of diabetic rats after using MNDF and intraperitoneal injection of insulin. Data are given as mean ± sd (n = 3). AUC: area under the plasma insulin curve over time; RBA: relative bioavailability compared with intraperitoneal injection. The RBA was calculated using the equation: RBA (%) = (AUC_{MNDF} × $dose_{IP}$)/(AUC_{IP} × $dose_{MNDF}$) × 100

Group	Dose	AUC 0 → 10 (h mU L^{-1})	RBA (%)
Injection insulin	5 U	91.60 ± 3.15	100
MNDF	5 U	89.62 ± 1.97	97.96 ± 5.52

Chondroitin sulfate ($W_{\text{Alg-ABA}} : W_{\text{CS}} = 1 : 1$) was mixed with Alg-ABA solution directly to form composites gels. To prepare the double layered structure, the gel containing the drug and 2 mg mL^{-1} GOD was first added to the mold and centrifuged to deposit on the needle tip. Then, the gel containing 0.04 mg mL^{-1} POD and 4 mg mL^{-1} TMB-HCl (2 mL) was loaded onto the mold. Finally, the microneedles were dried at room temperature. After being completely dried, the microneedles were divided into four parts, each containing 10 × 10 needle tips. The morphology of MNAP was obtained by scanning electron microscopy (SEM, SU8020).

Synthesis of biomineralized insulin

The synthesis of M-insulin was carried out as in a previous report.[30] Briefly, the mineralization of insulin was performed in DMEM at a temperature of 37 °C with 5% CO_2, and insulin (5 mg) was dissolved directly in DMEM (3 mL) and kept for 24 h to reach equilibrium. A total of 8.5 μL $CaCl_2$ (1 M) was introduced into the reaction mixture for incubation for another 24 h. In order to adjust the gas exchange between the reaction system and the external environment in time, the reaction tube was sealed with perforated tin foil. After the reaction, the mineralized insulin was purified by centrifugal ultrafiltration (100k MWCO) and washed three times with DI water. The solid was lyophilized and stored at −20 °C before use. The morphology and the element distribution of M-insulin were observed with a transmission electron microscope (TEM, JEM-1200EX). Then the composition of M-insulin was characterized by Fourier transform infrared (FTIR, Nicolet IS 5) spectroscopy.

Stability of mineralized insulin embedded in the MNDF

To evaluate the stability of mineralized insulin (M-insulin) embedded in the MNDF, the following four groups of M-insulin contents were measured with a Bradford Protein Assay kit to determine its biological activity: unprocessed M-insulin before and after storage at 37 °C for 12 h, M-insulin mixed with the Alg-ABA/CS complex before and after storage at 37 °C for 12 h, and M-insulin loaded in MNDF before and after storage at 37 °C for 12 h and 24 h.

Cytotoxicity test of MNDF

The *in vitro* cytotoxicity test was performed by a cell counting Kit-8 (cck-8) assay in Huvec. Huvec were seeded in a 96-well plate at a density of 8000 cells per well and cultivated in 100 μL of RPMI 1640 medium. The wells were grouped according to the difference in concentrations (0, 0.2, 0.4, 0.6, 0.8, 1.0 and 1.2 mg mL^{-1}, respectively) of the MNDF composite solution, each group including three wells. The plates were incubated at 37 °C in a CO_2 (5%) incubator for 24 h before administration. After 24 h of dosing incubation, the original culture medium was aspirated, and 100 μL cck-8 solution (10%) was added. The plates were incubated for an additional 2 h. The absorbance of the plates was read at a reference wavelength of 450 nm using a microplate reader (SPARK 10 M, TECAN) within 10 min.

In vitro discoloration and insulin release

To evaluate the *in vitro* color readout of the MNDF in response to different glucose levels, we fabricated agarose gels with different glucose concentrations to simulate the interstitial fluid extraction process. On inserting the microneedles into the agarose gels a change of the MNDF color was observed with glucose concentration and time. Around 400 μg GOD and 300 μg M-ins mineralized particles were integrated with the microneedle. Simultaneously, a blank microneedle only containing GOD was also fabricated. The release rate of insulin was assessed at three different glucose concentrations. The combination systems were exposed to different glucose solutions (1 mL) for a period of time. At each time point, a 5 μL supernatant was collected and the total protein content concentration or blank group GOD concentration was determined with a Bradford Protein Assay kit, and the insulin content was calculated using the following equation:

$$C_{(\text{insulin})} = C_{(\text{total protein})} - C_{(\text{GOD})}.$$

Animals

All animal procedures were performed in accordance with the Guidelines for Care and Use of Laboratory Animals of Nanjing University of Chinese Medicine and approved by the Animal Ethics Committee of Nanjing University of Chinese Medicine (202009A041).

Skin recovery post MNDF treatment

To validate the insertion and transdermal delivery capabilities of MNDF, FITC-insulin loaded in MNDF was applied for 10 min on the pig skin that was separated and wiped with 75% alcohol. The skin tissue from a frozen slice was used to observe the depth of the fluorescence signal. In order to explore the skin recovery ability after MNDF implantation *in vivo*, the backs of SD rats were shaved and wiped with 75% ethanol, then the MNDF was pressed on the skin for 10 min, and the recovery of the skin after removal was observed.

Establishment of the type 1 diabetes rat model

Rats were housed in plastic cages under controlled conditions (lighting from 07:00 to 19:00, 22 ± 1 °C surrounding temperature, 12 h/12 h light/dark cycle). The animals were randomly assigned to six groups: diabetes SD rats treated with intraperitoneal injection (5 U), diabetes SD rats treated with MNDF (5, 10 and 20 U), diabetes SD rats treated with blank MNDF (control group) and a healthy group. There were 4 rats in each group. Diabetic rats were induced with 80 mg kg^{-1} streptozotocin (STZ). All SD rats were fasted for 18 hours before intraperitoneal injection of streptozotocin (STZ), and they were allowed to drink freely.

Sample collection

Blood samples collected from the fundus venous plexus were measured with a glucose meter and then used for correlative

plasma insulin concentration analysis. The blood glucose levels of each rat were monitored per hour after administration (lasting for 6 h). The plasma was isolated and stored at −20 °C until it was assayed with an insulin ELISA kit. The RBA was calculated using the equation:

$$\text{RBA}\ (\%) = (\text{AUC}_{\text{MNDF}} \times \text{dose}_{\text{IP}})/(\text{AUC}_{\text{IP}} \times \text{dose}_{\text{MNDF}}) \times 100.$$

Meanwhile, to ensure sufficient contact of the interstitial liquid with the MNDF, the microneedle was inserted into the rat's skin and kept in place for 1 h, and pressed firmly for the first 1 min for easy penetration through the epidermis; a color change would occur in this hour for MNDF of hyperglycemic rats.

Histopathological analysis

The pancreas was placed in 4% paraformaldehyde. The samples were sectioned and stained with hematoxylin–eosin after embedding and examined under a light microscope. The kidney was put in 4% paraformaldehyde. The samples were sectioned and stained with periodic acid dye after embedding and examined under a light microscope. The preparation of tissue sections was technologically assisted by Wuhan Servicebio Technology Co., Ltd (China).

Color coordinate readout algorithm

According to the CIE chromaticity standard, the color gamut is composed of x and y values. The color gamut defines all colors that can be displayed and seen with the human eye from a specific output device. First, the RGB triplet color of each image was obtained, and the average value of non-linear RGB pixel values was calculated:

$$\text{R}_\text{a} = (\text{R}/255)$$

$$\text{G}_\text{a} = (\text{G}/255)$$

$$\text{B}_\text{a} = (\text{B}/255)$$

where R, G, and B are non-linear RGB pixel values, and R_a, G_a, and B_a are average values. Then, these values were linearized:

$$\text{R}_\text{l} = \{(\text{R}_\text{a} + 0.055)/1.055\}^{2.4}$$

$$\text{G}_\text{l} = \{(\text{G}_\text{a} + 0.055)/1.055\}^{2.4}$$

$$\text{B}_\text{l} = \{(\text{B}_\text{a} + 0.055)/1.055\}^{2.4}$$

among them, R_l, G_l, and B_l are linearized values. Next, the tristimulus values X, Y, and Z were calculated:

$$X = \text{R}_\text{l} \times 0.4124 \times 100 + \text{G}_\text{l} \times 0.3576 \times 100 + \text{B}_\text{l} \times 0.1805 \times 100$$

$$Y = \text{R}_\text{l} \times 0.2126 \times 100 + \text{G}_\text{l} \times 0.7152 \times 100 + \text{B}_\text{l} \times 0.0722 \times 100$$

$$Z = \text{R}_\text{l} \times 0.0193 \times 100 + \text{G}_\text{l} \times 0.1192 \times 100 + \text{B}_\text{l} \times 0.9505 \times 100$$

Finally, the X, Y, and Z values were converted to CIE 1931 color coordinate (x, y) values:

$$x = X/(X + Y + Z)$$

$$y = Y/(X + Y + Z).$$

Conclusions

In summary, a hierarchically structured MNDF for real-time glycemia sensing and self-regulated release of insulin has been developed *via* a micro-molding method. The MNDF consisted of a tip part for insulin release and a base surface for real-time glycemia sensing. The mineralized M-insulin particle enables long-acting release of insulin. The H^+ generated in the catalytic reaction of GOD and glucose gradually dissolves the calcium layer of M-insulin particles, resulting in self-regulated release of insulin. Elevating the levels of H_2O_2 brings about a visible color change allowing the glucose level to be read out. What's more, this design enables action as an active filter to scavenge superfluous H_2O_2, avoiding possible damage to normal tissues caused by oxidative stress. The MNDF is a promising device for practical application as a theranostic platform for self-regulated release of insulin and continuous glycemia monitoring.

Conflicts of interest

There are no conflicts to declare.

Acknowledgements

This work was supported by the Project of National Natural Science Foundation of China (81573388). We also greatly appreciate the financial support by the "Six Talent Peaks Project of Jiangsu Province (YY-032)" and the Open Project of Chinese Materia Medica First-Class Discipline of Nanjing University of Chinese Medicine (No. 2020YLXK025).

References

1 W. T. Cefalu, E. G. Berg, M. Saraco, M. P. Petersen, S. Uelmen, S. Robinson and A. Amer Diabet, *Diabetes Care*, 2019, **42**, S13–S28.
2 O. Veiseh, B. C. Tang, K. A. Whitehead, D. G. Anderson and R. Langer, *Nat. Rev. Drug Discovery*, 2015, **14**, 45–57.
3 A. B. Meneguin, A. L. P. Silvestre, L. Sposito, M. P. C. de Souza, R. M. Sabio, V. H. S. Araujo, B. S. F. Cury and M. Chorilli, *Carbohydr. Polym.*, 2021, **256**, 117504.
4 Y. Ohkubo, H. Kishikawa, E. Araki, T. Miyata, S. Isami, S. Motoyoshi, Y. Kojima, N. Furuyoshi and M. Shichiri, *Diabetes Res. Clin. Pract.*, 1995, **28**, 103–117.

5 P. Saeedi, I. Petersohn, P. Salpea, B. Malanda, S. Karuranga, N. Unwin, S. Colagiuri, L. Guariguata, A. A. Motala, K. Ogurtsova, J. E. Shaw, D. Bright, R. Williams, R. Almutairi, P. A. Montoya, A. Basit, S. Besancon, C. Bommer, W. Borgnakke, E. Boyko, J. Chan, H. Divakar, A. Esteghamati, N. Forouhi, L. Franco, E. Gregg, M. Hassanein, C. Ke, D. Levitt, L.-L. Lim, G. D. Ogle, D. Owens, M. Pavkov, J. Pearson-Stuttard, A. Ramachandran, W. Rathmann, M. Riaz, D. Simmons, A. Sinclair, E. Sobngwi, R. Thomas, H. Ward, S. Wild, X. Yang, L. Yuen, P. Zhang and I. D. F. D. A. Comm, *Diabetes Res. Clin. Pract.*, 2019, **157**, 107843.
6 Y. Zhang, J. Yu, A. R. Kahkoska, J. Wang, J. B. Buse and Z. Gu, *Adv. Drug Delivery Rev.*, 2019, **139**, 51–70.
7 S. P. Narayanan and S. Raghavan, *Int. J. Adv. Manuf. Technol.*, 2017, **93**, 407–422.
8 A. Matsumoto, M. Tanaka, H. Matsumoto, K. Ochi, Y. Moro-oka, H. Kuwata, H. Yamada, I. Shirakawa, T. Miyazawa, H. Ishii, K. Kataoka, Y. Ogawa, Y. Miyahara and T. Suganami, *Sci. Adv.*, 2017, **3**(11), eaaq0723.
9 S.-H. Baek, J.-H. Shin and Y.-C. Kim, *Biomed. Microdevices*, 2017, **19**(1), 2.
10 H. Jun, M.-R. Han, N.-G. Kang, J.-H. Park and J. H. Park, *J. Controlled Release*, 2015, **207**, 1–6.
11 J. Arya, S. Henry, H. Kalluri, D. V. McAllister, W. P. Pewin and M. R. Prausnitz, *Biomaterials*, 2017, **128**, 1–7.
12 Y.-C. Kim, J.-H. Park and M. R. Prausnitz, *Adv. Drug Delivery Rev.*, 2012, **64**, 1547–1568.
13 I. C. Lee, W.-M. Lin, J.-C. Shu, S.-W. Tsai, C.-H. Chen and M.-T. Tsai, *J. Biomed. Mater. Res., Part A*, 2017, **105**, 84–93.
14 K.-Y. Seong, M.-S. Seo, D. Y. Hwang, E. D. O'Cearbhaill, S. Sreenan, J. M. Karp and S. Y. Yang, *J. Controlled Release*, 2017, **265**, 48–56.
15 C. Wang, Y. Ye, W. Sun, J. Yu, J. Wang, D. S. Lawrence, J. B. Buse and Z. Gu, *Adv. Mater.*, 2017, **29**(18), 1606617.
16 D. H.-C. Chou, M. J. Webber, B. C. Tang, A. B. Lin, L. S. Thapa, D. Deng, J. V. Truong, A. B. Cortinas, R. Langer and D. G. Anderson, *Proc. Natl. Acad. Sci. U. S. A.*, 2015, **112**, 2401–2406.
17 J. Wang, J. Yu, Y. Zhang, X. Zhang, A. R. Kahkoska, G. Chen, Z. Wang, W. Sun, L. Cai, Z. Chen, C. Qian, Q. Shen, A. Khademhosseini, J. B. Buse and Z. Gu, *Sci. Adv.*, 2019, **5**(7), eaaw4357.
18 Q. Wu, L. Wang, H. Yu, J. Wang and Z. Chen, *Chem. Rev.*, 2011, **111**, 7855–7875.
19 J. Yu, J. Wang, Y. Zhang, G. Chen, W. Mao, Y. Ye, A. R. Kahkoska, J. B. Buse, R. Langer and Z. Gu, *Nat. Biomed. Eng.*, 2020, **4**, 499–506.
20 X. Hu, J. Yu, C. Qian, Y. Lu, A. R. Kahkoska, Z. Xie, X. Jing, J. B. Buse and Z. Gu, *ACS Nano*, 2017, **11**, 613–620.
21 C. Li, X. Liu, Y. Liu, F. Huang, G. Wu, Y. Liu, Z. Zhang, Y. Ding, J. Lv, R. Ma, Y. An and L. Shi, *Nanoscale*, 2019, **11**, 9163–9175.
22 Z. Tong, J. Zhou, J. Zhong, Q. Tang, Z. Lei, H. Luo, P. Ma and X. Liu, *ACS Appl. Mater. Interfaces*, 2018, **10**, 20014–20024.
23 J. Yu, C. Qian, Y. Zhang, Z. Cui, Y. Zhu, Q. Shen, F. S. Ligler, J. B. Buse and Z. Gu, *Nano Lett.*, 2017, **17**, 733–739.
24 J. Yu, Y. Zhang, Y. Ye, R. DiSanto, W. Sun, D. Ranson, F. S. Ligler, J. B. Buse and Z. Gu, *Proc. Natl. Acad. Sci. U. S. A.*, 2015, **112**, 8260–8265.
25 J. Wang, Z. Wang, J. Yu, A. R. Kahkoska, J. B. Buse and Z. Gu, *Adv. Mater.*, 2020, **32**(13), 1902004.
26 G. Saravanakumar, J. Kim and W. J. Kim, *Adv. Sci.*, 2017, **4**(1), 1600124.
27 J. Lee, S. H. Park, I. H. Seo, K. J. Lee and W. Ryu, *Eur. J. Pharm. Biopharm.*, 2015, **94**, 11–19.
28 W. Chen, R. Tian, C. Xu, B. C. Yung, G. Wang, Y. Liu, Q. Ni, F. Zhang, Z. Zhou, J. Wang, G. Niu, Y. Ma, L. Fu and X. Chen, *Nat. Commun.*, 2017, **8**, 1–11.
29 H. Meng, P. Xiao, J. Gu, X. Wen, J. Xu, C. Zhao, J. Zhang and T. Chen, *Chem. Commun.*, 2014, **50**, 12277–12280.
30 W. Chen, G. Wang, B. C. Yung, G. Liu, Z. Qian and X. Chen, *ACS Nano*, 2017, **11**, 5062–5069.

